Journal of Materials Processing Tech. 288 (2021) 116880

Contents lists available at ScienceDirect

Journal of Materials Processing Tech.

journal homepage: www.elsevier.com/locate/jmatprotec

# Enhanced combination of mechanical properties and electrical conductivity of a hard state Cu-Cr-Zr alloy via one-step friction stir processing

Y.D. Wang[a,b], M. Liu[a,b], B.H. Yu[a], L.H. Wu[a], P. Xue[a,*], D.R. Ni[a,*], Z.Y. Ma[a]

[a] Shenyang National Laboratory for Materials Science, Institute of Metal Research, Chinese Academy of Sciences, 72 Wenhua Road, Shenyang 110016, China
[b] School of Materials Science and Engineering, University of Science and Technology of China, 72 Wenhua Road, Shenyang 110016, China

ARTICLE INFO

Associate Editor: R Mishra

*Keywords:*
Cu-Cr-Zr alloy
friction stir processing
ultrafine grains
tensile strength
electrical conductivity

ABSTRACT

How to coordinate the strength, ductility and electrical conductivity of Cu-Cr-Zr alloys has always been a difficult problem. Unlike most of previous reports on processing soft state (solution state) alloys, in the present study, a hard state (aged state) Cu-Cr-Zr alloy was subjected to one-step friction stir processing (FSP) at room temperature with more attentions paid to the evolution of grains and precipitates, and their effects on the mechanical and electrical properties. The results showed that the precipitates played a key role in grain refinement, and ultrafine grains (UFG) with an average size of 250 nm were produced after FSP. Many fine precipitates (average size of 3.1 nm) were uniformly distributed in the grains, neither dissolved nor obviously coarsened. Excellent comprehensive properties of high tensile strength (702 MPa), good elongation (16%) and electrical conductivity (74.3% IACS) were achieved in the FSP sample. Furthermore, this one-step FSP method does not need subsequent aging treatment which is indispensable for conventional processing methods, providing a simplified and efficient method for improving the performance of Cu-Cr-Zr alloys.

## 1. Introduction

Copper and its alloys are the most widely used conductive materials because of their excellent conductivity, high strength, and good ductility. With the rapid developments in the power, electronic and electromagnetic fields, advanced equipment, such as high-speed railway contact wire (Liu et al., 2006) and spot-welding electrode (Kulczyk et al., 2018), are increasingly demanding high-strength and high-conductivity metals with good ductility. However, how to coordinate the strength, ductility and electrical conductivity of metals has always been a difficult problem: the previous used methods to improve strength via creating various crystal defects would inevitably deteriorate the conductivity and ductility, confirmed by Lu et al. (2004).

Considering the different degrees of conductivity reduction caused by various crystal defects mentioned by Li et al. (2007), Cu-Cr-Zr alloys are desired high strength and high conductivity material constructed by nanoscale precipitates and low-solute-content matrix. Shangina et al. (2017) demonstrated that tiny alloying element addition (~1 wt.%) can significantly increase the strength while minimally lose the conductivity compared to that of the pure copper. Chembarisova et al. (2020) identified that the dissolution of Cr or Zr atoms in Cu matrix was the most significant factor to damage the conductivity. To further improve the strength, Cu-Cr-Zr alloys were usually processed by a long trilogy under soft condition: severe plastic deformation (SPD) such as equal channel angular pressing (ECAP) conducted by Liang et al. (2018), high pressure torsion (HPT) conducted by Purcek et al. (2020), along with preceding solution treatment and subsequent aging treatment. Chen et al. (2019) presented the need to simplify the processing route of Cu-Cr alloy. What's more, Cu-Cr-Zr alloys produced by SPD usually exhibit limited ductility. For instance, Zhang et al. (2017) reported that due to the lack of ability to accumulate dislocations, the total elongation of Cu-Cr-Zr alloy after cryorolling reduced to 1.2%.

Friction stir processing (FSP), a potential SPD technique, made it possible to obtain equiaxed UFG microstructure with better matching of strength and ductility (Mishra and Ma, 2005). Recently, Wang et al. (2019) processed a soft state Cu-Cr-Zr alloy via cryogenic FSP technology, achieving an interesting matching of high (UTS, 840 MPa) and good electrical conductivity (89% IACS). However, the performance advantages obtained via this extreme process are overshadowed by the very low elongation (~2%) and the additional solution and aging processes. On the other hand, previous studies on FSP of hard state Cu-Cr-Zr alloys showed that the strength and conductivity were sharply reduced. Jha et al. (2017) imposed FSP on an aged state Cu-Cr-Zr alloy under rotation rate of 1200 rpm. As a result, the UTS reduced to only 255 MPa. Lai et al. (2018) processed an aged state Cu-Cr-Zr alloy via FSP with rotation rate of 1500 rpm and tool shoulder 40 mm in

* Corresponding authors.
*E-mail addresses:* pxue@imr.ac.cn (P. Xue), drni@imr.ac.cn (D.R. Ni).

https://doi.org/10.1016/j.jmatprotec.2020.116880
Received 28 March 2020; Received in revised form 7 August 2020; Accepted 16 August 2020
Available online 19 August 2020
0924-0136/ 

diameter, which result in the hardness and electrical conductivity reduced to 50% and 70% of that of the base material (BM), respectively. The main reason for the property degradation was the coarsening and dissolution of nanoscale precipitates under the excessive heat input adopted in those processes.

Therefore, greatly decreasing the heat input during FSP should be a good method to enhance the strength of the aged state Cu-Cr-Zr alloy with good ductility and conductivity, and this method has three advantages. Firstly, it could ensure that the nanoscale precipitates neither coarsened nor dissolved, thereby maintaining the precipitation strengthening effect and the good conductivity. Secondly, Wu et al. (2019) showed that the growth of the recrystallized grain could be inhibited by the decreased heat input, which further enhanced the strength by grain refining. Lastly, the reserved precipitates in the matrix was also beneficial to grain refinement, because they could facilitate nucleation by providing more nucleation sites and inhibiting grain growth, which was demonstrated by Pippan et al. (2006). The adding of aging process before solution state Cu-Cr-Zr alloys subjected to 4 passes ECAP successfully refined the grains from 144 nm to 85 nm in León et al. (2012), which also demonstrated the benefit of precipitates on grain refinement.

It is noted that, for the SPD processes of Cu-Cr-Zr alloys, few researchers have paid attention to the positive effect of the precipitates: either conducting plastic deformation under soft condition, or applying large-heat-input deformation that resulted in the coarsening and dissolution of the precipitates, losing their grain refinement function. In addition, preserving precipitates during FSP means that conventional solution treatment before SPD and subsequent aging treatment can be omitted. This simplified one-step FSP can improve the production efficiency, which is beneficial for industry manufacture.

In the present study, a hard state Cu-Cr-Zr alloy was subjected to one-step FSP under low heat input for the first time, and the effect of microstructure evolution, including precipitates and grain size, on the electrical conductivity, hardness and tensile properties of the Cu-Cr-Zr alloy was studied in detail. The aim of this study is to realize an enhanced combination of mechanical property and electrical conductivity of the Cu-Cr-Zr alloy by a simple one-step FSP.

## 2. Material and methods

5 mm thick hard state (peak aged state) commercial Cu-0.83Cr-0.14 Zr (wt.%) alloy plates were prepared by casting, hot-forging followed by quenching and aging. These plates were chosen as the BM for FSP at room temperature. The stir tool was made of W-Re alloy, with a small shoulder 11 mm in diameter, a taper pin 1.8 mm in length and 5 mm in root diameter. Three low rotation rates, i.e., 300 rpm, 400 rpm and 600 rpm, were selected, and the corresponding samples were designated as R300 sample, R400 sample and R600 sample, respectively. For both FSP processes, the travel speed, tilt angle of the tool and the plunge depth of the tool shoulder were 50 mm/min, 3˚, and 0.2 mm, respectively. At the lowest rotation rate of 300 rpm, tunnel defects appeared and the stir tool fractured. Therefore, just the R400 and R600 samples were carefully investigated in this study. Low heat input was guaranteed by such tool dimension and processing parameters. Two thermocouples were respectively placed on the advancing side (AS) and retreating side (RS), at 2.5 mm from the center of the stir zone (SZ), to simultaneously record the thermal cycle during FSP. In order to verify whether there was obvious dissolution of the nanoscale precipitates, an aging treatment at 480 ˚C for 15 ~ 100 min was conducted after FSP. The BM samples were solution treated at 960 ˚C for 2 h and then quenched into water as control group to the same aging treatment.

Microstructural observation and analysis were conducted on optical microscope (OM), scanning electron microscope (SEM, ZEISS, Supra 55) equipped with an electron backscattering diffraction (EBSD, HKL, Channel 5 type) analyzer. All specimens for OM and EBSD observation were machined perpendicular to the processing direction by electro discharge cutting machine. After grinding and polishing, the specimens for OM observation were etched in a solution of 100 ml $H_2O$ + 10 ml HCl +5 g $FeCl_3$, and specimens for EBSD observation were electropolished using 5 V direct current in a solution of 25 ml $(CH_3)_2CHOH$ + 125 ml $H_3PO_4$ + 125 ml $C_2H_5OH$ + 250 ml $H_2O$ + 2.5 g $(NH_2)_2CO$ at about −10 ˚C. EBSD observation was conducted at a step size of 30-40 nm. More detailed microstructure of the SZs and BM were further examined by transmission electron microscope (TEM, FEI, Tecnai G2 F20). The TEM foils 3 mm in diameter were prepared by twin-jet electropolishing techniques in a solution of 300 ml $HNO_3$ + 700 ml $CH_2OH$ at about −30 ˚C.

Vickers microhardness measurement was conducted on the cross-section perpendicular to the processing direction in the SZs with an applied load of 200 g and a holding time of 15 s. Dog-bone-shaped tensile specimens with a gauge length of 5 mm and cross-section area of 2 mm × 1 mm were prepared parallel to the processing direction, and tested at room temperature on Instron 5848 testing machine with an initial strain rate of $10^{-3}$ $s^{-1}$.

The electrical conductivity at room temperature was tested on D60 K eddy-current electrical conductivity instrument and TH2515 DC Resistance Tester, and the resistance value was converted into the electrical conductivity. The specimens for electrical conductivity tests were machined parallel to the processing direction and ground to a dimension of 10 mm (length) × 2 mm (width) × 2 mm (thickness).

## 3. Results and discussion

### 3.1. Microstructure evolution

Fig. 1 shows the typical cross-sectional macrographs of R600 and R400 samples. The SZs of both samples had similar profiles. Zeng et al. (2019) showed the conventional basin-shaped SZs with wide top regions formed by FSP with large heat input, while the shoulder affected zones in the present FSP samples were very small. This phenomenon is believed to be caused by the insufficient material flow due to the low FSP heat input, high thermal conductivity and high deformation resistance of Cu-Cr-Zr alloy.

The temperature histories on both sides of the SZs for the R600 and R400 samples are shown in Fig. 2. The peak temperature on the AS was as high as 428 ˚C for R600 sample, but decreased to only about 240 ˚C for R400 sample. Thus, decreasing rotation rate is an effective strategy to decrease the peak temperature during FSP. Considering the simulated temperature distributions in the Cu-Cr-Zr alloy plates during FSW by Lai et al. (2018), the temperature in SZ center would be no more than 50 ˚C higher than that at the monitoring point during FSP. Therefore, the peak temperature in SZ centers of R600 and R400 samples would be lower than 480 ˚C and 290 ˚C, respectively. Jha et al. (2017) detected the thermal cycle during FSP Cu-Cr-Zr alloy with thermocouples, the peak temperature on the AS was higher than that on the RS and exceeded to 800 ˚C. Similarly, the peak temperatures on the

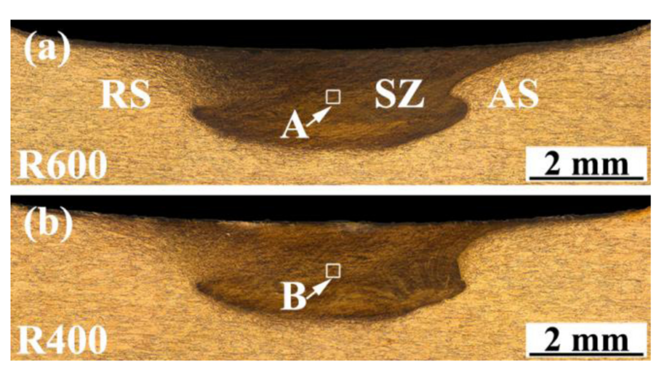


**Fig. 1.** Typical cross-sectional macrographs of FSP Cu-Cr-Zr alloy: (a) R600 sample and (b) R400 sample.

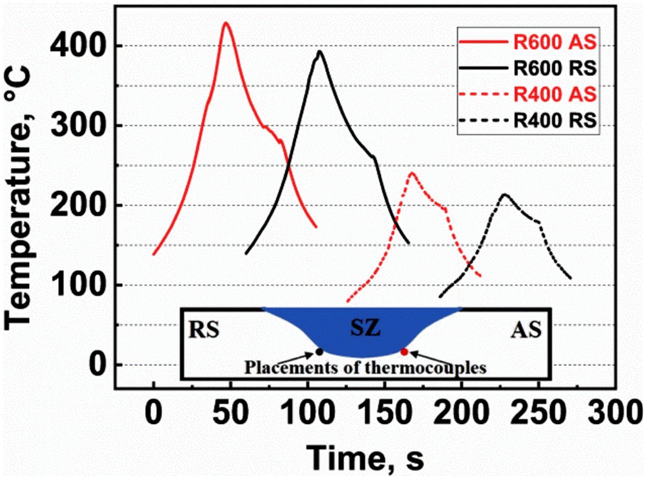


**Fig. 2.** Thermal cycles on both side of SZs in R600 and R400 samples (the inserted schematic showing the thermocouple locations).

AS were about 36 °C and 26 °C higher than those on the RS for R600 sample and R400 sample in this study, respectively. Differently, such a low heat input for R400 sample is the basis of grain refinement and preventing the precipitates from dissolving and coarsening.

The microstructures in the SZs of R600 and R400 samples (positions A, B shown in Fig. 1) were analyzed via EBSD, and the inverse pole figure (IPF) maps, grain boundary (GB) misorientation distributions and pole figures for both samples are shown in Fig. 3. The high angle GBs (HAGBs, misorientation angle ≥ 15°) and low angle GBs (LAGBs, misorientation angle < 15°) are depicted by black and white lines in IPF maps. The EBSD data in Xue et al. (2016) exhibited the typical microstructure of FSP Cu that characterized by fine grains with a typical equiaxed recrystallized microstructure. The microstructure of R600 sample composed of equiaxed grains with an average size of 420 nm were observed. Considering all the GBs with misorientation angles > 2°, the GB misorientation distribution in the SZ of R600 sample is close to the random distribution of a cubic metal. The fraction of HAGBs was as high as 90%, which indicates that nearly full recrystallization occurred in R600 sample. Differently, the grains in R400 sample are stretched along the rotation direction of the pin, and the fraction of HAGBs was relatively low (about 76% of the total GB length). What's more, the average grain size of R400 sample was 280 nm, which is much smaller than that of R600 sample. The finer elongated grains and low fraction of HAGBs indicate that the incompletely recrystallized fine grain structure was reserved in R400 sample, due to the relatively low heat input. Compared with the EBSD data of Cu-Cr-Zr alloys after ECAP in Mishnev et al. (2015), FSP can greatly refine the grains while maintain the high ratio of HAGBs.

The pole figures of the R600 and R400 samples with the relevant textures are shown in Fig. 3e and f, respectively. The TD and ND were transverse direction and normal direction of the FSP plates, respectively. Like textures in the SZ of FSP Cu-30Zn brass in Xu et al. (2018), the texture in R600 sample predominantly consisted of the $A/\overline{A}$ {1 1 1} ⟨1 1 0⟩ component with the maximum pole density value of 5.09, and the textures in the R400 sample mainly exhibited a {0 0 1} ⟨1 1 0⟩ orientation with the maximum pole density value of 4.77. Both the samples exhibited shear fiber textures. This character has a good agreement with the fact that ⟨1 1 0⟩ is the preferable orientation for the shear direction in the f.c.c. metals monotonically formed by simple shear deformation around the pin. Previous study of Xue et al. (2013) indicated that fiber texture with the maximum pole density value of 8.83 had no effect on mechanical properties. Therefore, the effect of the weak texture in this study on static load performance could be ignored.

Fig. 4 shows the OM and bright-field TEM images of the BM and FSP samples, and the statistical distributions of the grain sizes measured by the linear intercept method. The BM was mainly composed of equiaxed coarse grains with an average grain size of 76 μm (Fig. 4a). Considering the hot-forging and aging processes to prepare the BM, the dislocation density of BM would be very low. FSP caused a significant grain refinement and UFG structures with average grain sizes of 360 nm and 250 nm were obtained in the SZs of R600 and R400 samples, respectively (Fig. 4b and c). Xue et al. (2019) summarized the typical characteristics of HAGB after FSP: the GBs are sharp, clear, and relatively straight. A low dislocation density was observed in the equiaxed UFG structure of R600 sample, and most GBs were HAGBs. Compared to those in R600 sample, the grains were further refined in R400 sample and regularly arranged along the rotation direction of the pin which is in accord with that observed by EBSD in Fig. 3b. Moreover, some dislocation cell structures and wavy, diffuse, ill-defined low angle GBs, as indicated in Fig. 4d, were frequently observed in R400 sample, which are similar to those in SPD UFG Cu-Cr-Zr alloys observed in Purcek et al. (2020). Though these sub-structures formed in R400 sample, the dislocation density was still much less than that produced by SPD.

As shown in Fig. 5a, it was found that many nano-sized particles were uniformly distributed in the Cu matrix of the BM. Chen et al. (2018b) proved that these particles were Cr-rich precipitates with Cu and Cr, as well as a small amount of Zr contained in these solid solutions. The atom probe tomography date of Chbihi et al. (2012) showed that the Cr-rich precipitates coarsened with the aging time. Peng et al. (2017) observed that the aging precipitation process of the Cu-0.71 wt % Cr alloy aged at 450 °C is supersaturated solid solution → G.P. zones → f.c.c. Cr phase → order f.c.c. Cr phase → b.c.c. Cr phase. Therefore, two kinds of Cr-rich precipitates could be observed in the BM. The first one showed a typical coffee-bean shape, as shown by the black arrows in Fig. 5a. This type of precipitate was reported to be f.c.c. structure, and coherent (cube-on-cube orientation relationship) with the Cu matrix (Chen et al., 2018a). The second one showed an ellipse-like shape with a b.c.c. structure, which was believed to lose the coherent relationship with the Cu matrix (Chbihi et al., 2012), as shown by the white arrows in Fig. 5a. The size distributions of the precipitates in BM and FSP samples are shown in Fig. 5d. Compared to the precipitates in the BM with an average size of 2.8 nm, the precipitates in R600 sample were distinctly coarsened to 5.5 nm with the disappearance of the coffee-bean shaped precipitates, as shown in Fig. 5b. Differently, the average precipitate size (3.1 nm) in R400 sample was not obviously coarsened compared to that of the BM, and some of them still maintained the coffee-bean shape as shown by the black arrows in Fig. 5c, indicating their coherent relationship with the Cu matrix. With the increase of heat input during FSP, the precipitates gradually coarsened and lost the coherent relation with the Cu matrix, which is consistent with the precipitation sequence in Cu-Cr-Zr alloys.

Compared to the grain size in the FSP pure Cu (400 nm) with water cooling in Xue et al. (2013), the grains in the present FSP Cu-Cr-Zr alloy was smaller. On the other hand, Su et al. (2011) reported that the elongated grains in FSP pure Cu were only observed near the pin extraction site under dry ice cooling condition and it was believed that the early elongated crystallites quickly coarsened to equiaxed grain structures when passing FSP tool. However, in the present study, elongated grains with very fine size of 250 nm were acquired in Cu-Cr-Zr alloy via FSP without any external cooling conditions. Clearly, the precipitates in the Cu-Cr-Zr alloy played a key role in the microstructural evolutions. The nano-precipitates provided more nucleation sites and acted as strong obstacles to the dislocation motion during FSP, which can slow down the processes of grain growth. Therefore, the UFG structures with deformation-induced features that disappeared in conventional FSP pure Cu can be preserved in the present FSP Cu-Cr-Zr alloy with nano-precipitates.

It is well proved that the precipitates in the SZ went through a complex evolution involving coarsening, dissolution and re-precipitation processes under the effects of thermal cycle and plastic deformation during FSP (Yang et al., 2020). According to the equilibrium phase

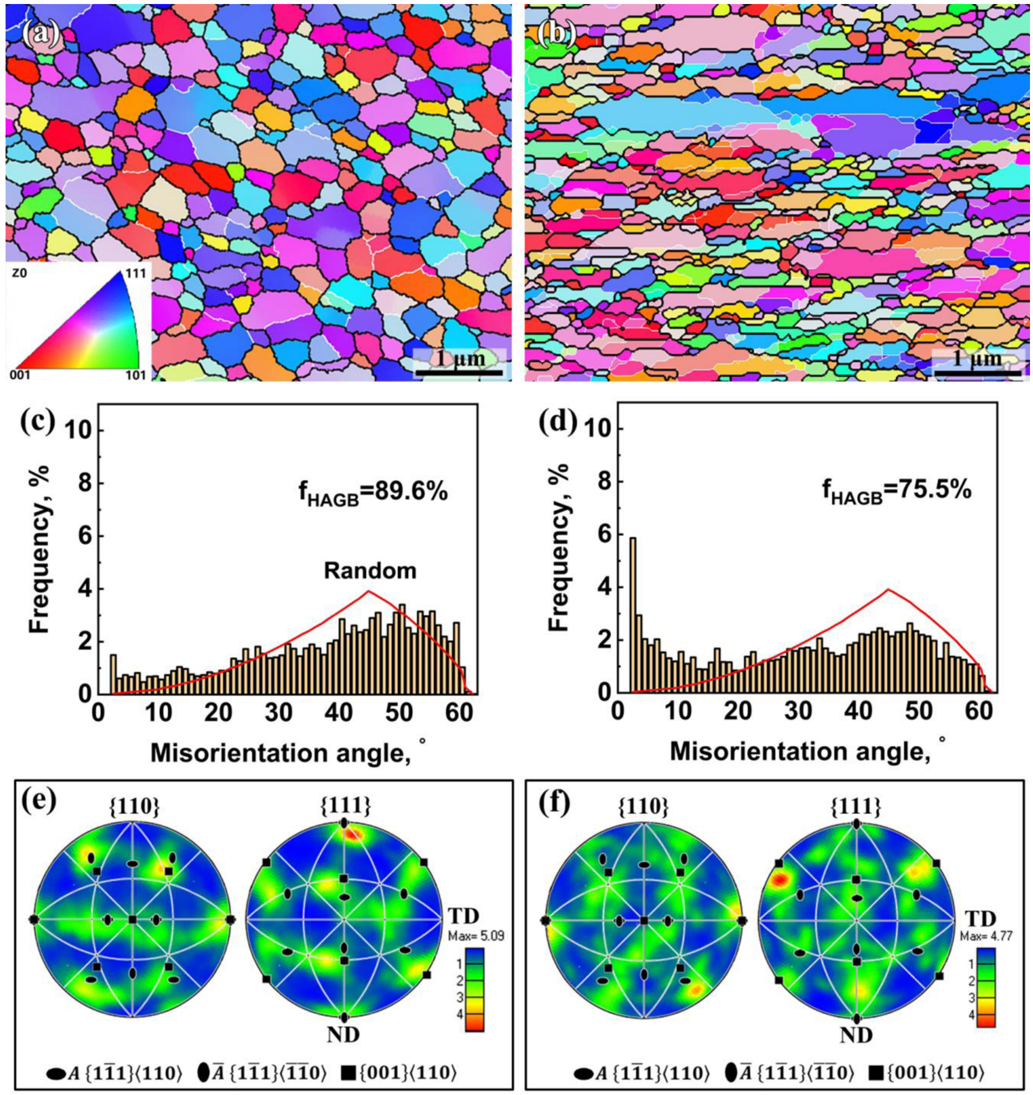


**Fig. 3.** EBSD images of the microstructure, IPF maps of (a) R600 sample and (b) R400 sample, GB misorientation distributions of (c) R600 sample and (d) R400 sample, and pole figures of (e) R600 sample and (f) R400 sample.

diagram in Chakrabarti and Laughlin (1984), the solubility of Cr in Cu increases with increasing temperature. Usually, the temperature for solution treatment of this alloy is at the range of 940 °C to 1020 °C. Under conventional FSP condition reported in Lai et al. (2018), most of the precipitates in Cu-Cr-Zr alloys could dissolve into the Cu matrix when the peak-temperature exceeded 800 °C with a following steep cooling rate. On the contrary, the peak-temperature at the monitoring site of R600 sample was 428 °C in this work, and it would be well below 800 °C in the SZ center considering the high thermal conductivity of the Cu-Cr-Zr alloy. In addition, the duration of temperature suitable for precipitation during the cooling process of FSP was much shorter than that in Lai et al. (2018) and Jha et al. (2017). Hence, just a small fraction of the precipitates dissolved into the Cu matrix and the reserved precipitates in R600 sample were just coarsened and lost the coherent relationship with the Cu matrix, rather than dissolved and precipitated again during the FSP process. The peak-temperature at the monitoring site of R400 sample was only 240 °C, much lower than that of R600 sample. Therefore, the activation energy for precipitate growth and transformation driven by temperature was insufficient. Thus, the precipitates in R400 sample were not obviously coarsened, and part of them maintained the coherent relationship with the Cu matrix. Because of the peak temperature in the SZ of R400 sample was far lower than the solution temperature of Cu-Cr-Zr alloys, precipitates scarcely dissolved into the Cu matrix.

### 3.2. Mechanical properties

Fig. 6 shows the hardness distributions in the SZs of R600 and R400 samples and the average hardness of the BM and FSP samples are summarized in Table 1. Owing to the significant grain refinement, the average hardness value in the SZ of R600 sample increased from 151 HV to 168 HV. The average hardness value further increased to 196 HV in the SZ of R400 sample, due to the finer grains and reserved precipitates under the relatively low heat input condition. The variation of microhardness can reflect the changes in microstructure. Xue et al. (2016) investigated the microstructure and hardness in the different positions of the FSP Cu under a very low heat input condition with water cooling, and concluded that the microstructure was homogeneous in the SZ. Similarly, the differences of hardness values were very small in various areas of the SZ (Fig. 6), so the microstructure of FSP Cu-Cr-Zr alloys should be relatively uniform in the SZ.

The engineering stress-strain curves of the BM and FSP samples are shown in Fig. 7, and the tensile properties are summarized in Table 1. For the BM, the yield strength (YS) and UTS were 417 MPa and 463 MPa, respectively, and the total elongation was over 30%. It can be seen that the tensile properties of the FSP samples were sensitive to the heat

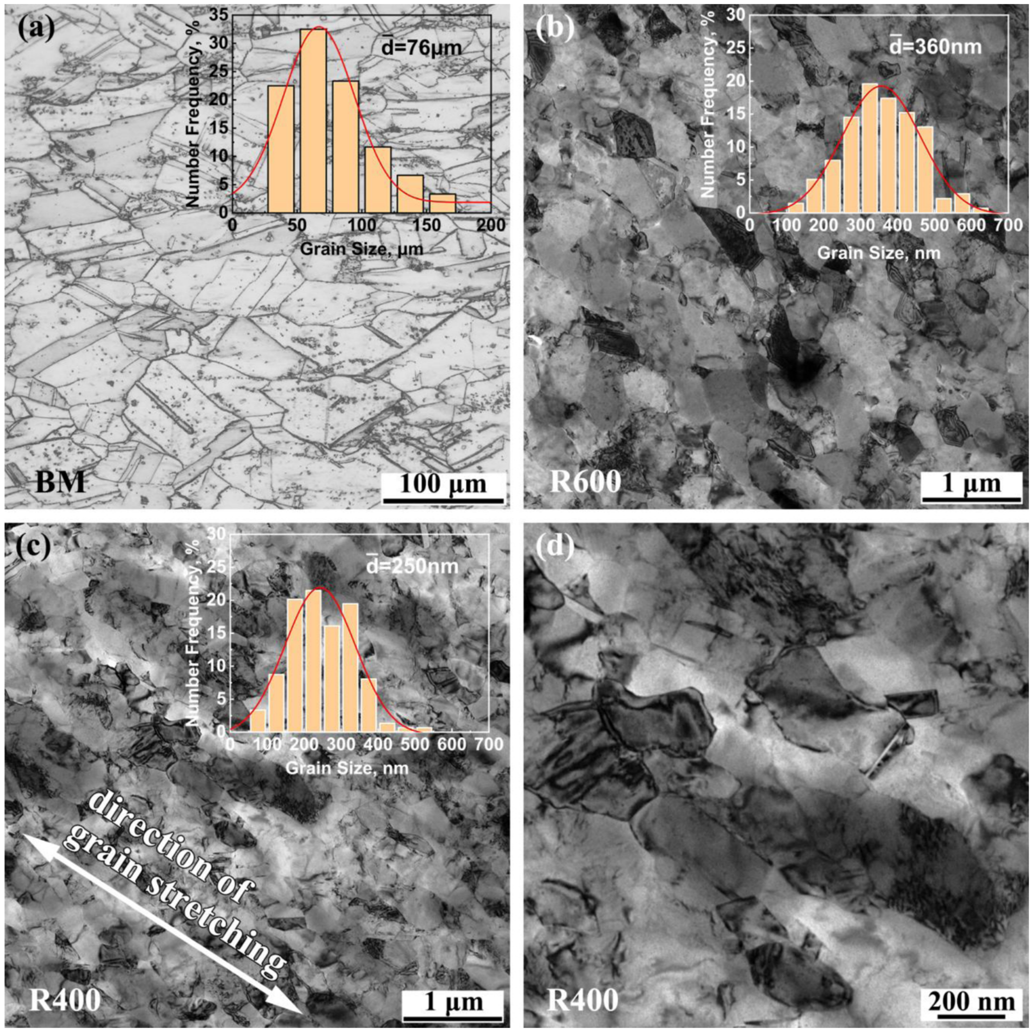


**Fig. 4.** (a) OM image of BM, and bright-field TEM images of (b) R600, (c) R400 samples with histograms showing the grain size distributions, and (d) typical magnified micrograph of R400 sample.

input determined by the rotation rate. Compared to the BM, the YS and UTS of R600 sample increased to 540 MPa and 580 MPa, respectively, and the total elongations decreased to 15%. With further decreasing the heat input, FSP resulted in a more notable increase in the mechanical characteristics ($\sigma_{YS}$ =620 MPa and $\sigma_{UTS}$ =702 MPa) of R400 sample, whereas the total elongation increased slightly to 16% compared to that of the R600 sample, exhibiting the highest comprehensive mechanical properties.

The tensile curves of FSP Cu-Cr-Zr samples show the typical features of SPD UFG metals with high strength but low uniform elongation. However, compared with the previously reported results in Sun et al. (2015) and Wang et al. (2019) of SPD Cu-Cr-Zr alloys (usually less than 5% total elongation) with the same gauge length of 5 mm, the 16% total elongation of R400 sample is very attractive. Xue et al. (2016) found that because of the characteristic of equiaxed grains with low dislocation density, high fraction of HAGBs and weak texture, the strain hardening capacity of FSP Cu was higher than that of the SPD Cu. Similarly, in present work, the microstructures of the SZs were featured with high HAGB ratios and low dislocation density (Fig. 3 and Fig. 4c, d). Thus, in the process of tensile plastic deformation, dislocations could be effectively stored near the HAGBs, and the strain hardening ability was improved, which is favorable for obtaining good ductility and confirmed by. Furthermore, as reported in Zhao et al. (2010), HAGB slip or associated GB activity may occur in UFG materials, which also contributes to the improvement of the elongation.

It is well accepted that the YS of Cu alloys can be calculated by Eq. (1), assuming that the different strengthening mechanisms are independent of each other (Liang et al., 2018).

$$\sigma_{YS} = \sigma_0 + \sigma_{solid\ solution} + \sigma_{precipitate} + \sigma_{grain\ boundary} + \sigma_{dislocation} \quad (1)$$

where $\sigma_0$ is intrinsic lattice stress, $\sigma_{solid\ solution}$ is solid solution strengthening stress, $\sigma_{precipitate}$ is precipitation strengthening stress, $\sigma_{grain\ boundary}$ is grain-boundary strengthening stress, and $\sigma_{dislocation}$ is dislocation strengthening stress.

Comparing the tensile behavior of the solid solution state Cu-Cr-Zr alloy in Purcek et al. (2016) and the fully annealed pure Cu in Xue et al. (2016), it can be found that the solid solution strengthening effect is very weak by the Cr and Zr atoms. When considering the grain-boundary strengthening, the added value is quantified by Hall-Petch relation estimated by Eq.(2), and Chen et al. (2006) proved that Hall-Petch relation is still valid for UFG Cu alloys by drawing a hardness-grain size graph in the range of nanocrystalline Cu to CG Cu.

$$\sigma_{grain\ boundary} = K_{H-P} \bullet d^{-1/2} \quad (2)$$

where $K_{H-P}$ is the Hall-Petch coefficient, and $d$ is the effective grain size. As reported by Liang et al. (2018), $K_{H-P}$ = 0.129 MPa m$^{1/2}$. As mentioned earlier, the average grain sizes of R600, R400 and BM samples are 360 nm, 250 nm and 76 μm, respectively. So, the YS increment by the grain-boundary strengthening can be calculated by the following Eq.(3):

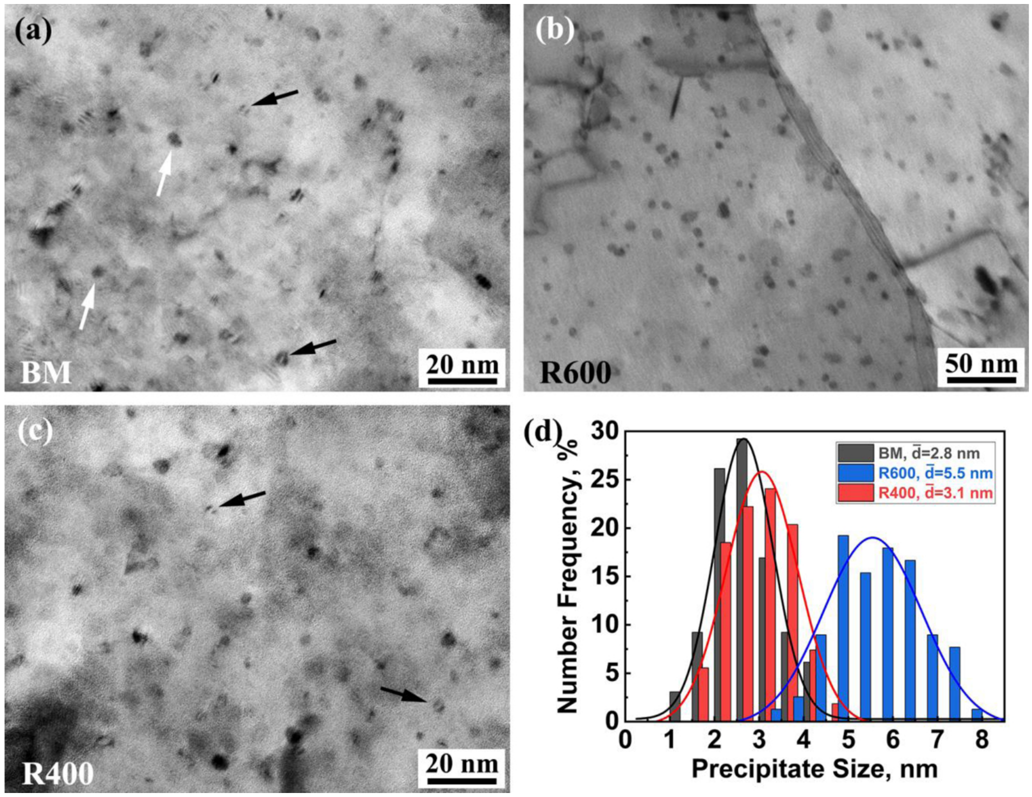


**Fig. 5.** Bright-field TEM images of precipitates in (a) BM, (b) R600 sample and (c) R400 sample, and (d) histogram showing the precipitate size distributions.

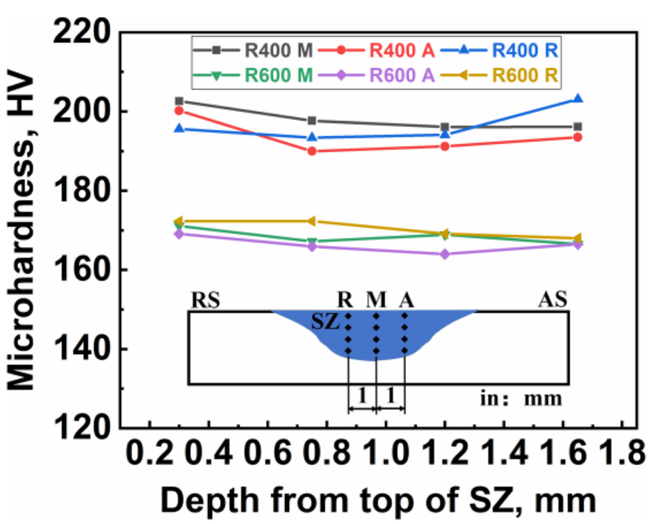


**Fig. 6.** Microhardness distribution in the SZs of R600 and R400 samples with the schematic showing the indentation locations.

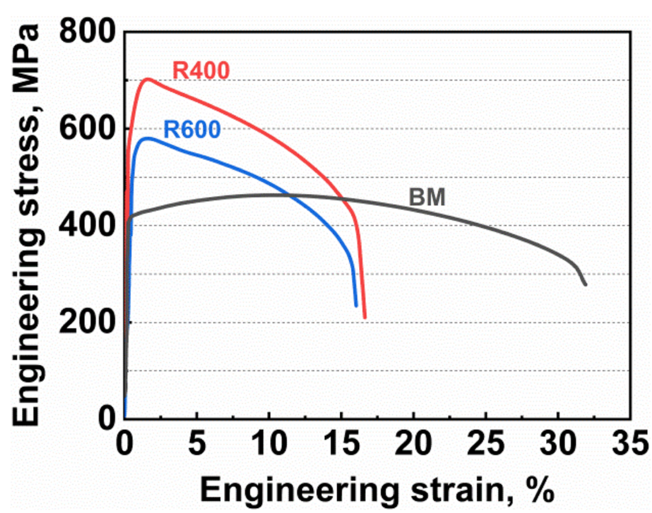


**Fig. 7.** Engineering stress-strain curves of BM and FSP samples.

$$\Delta\sigma_{grain\ boundary} = \sigma_{grain\ boundary,\ SZ} - \sigma_{grain\ boundary,\ BM} \quad (3)$$

Compared to the BM, the YS increment by the grain-boundary strengthening for R600 sample is calculated as 200 MPa, while the actual YS increment is just 123 MPa. Obviously, the coarsening and dissolution of precipitates resulted in the decreased part of YS. For R400 sample, the YS increment by the grain-boundary strengthening is calculated as 243 MPa, which is slightly lower than the actual YS increment (253 MPa). It is accepted that the increased dislocation density in R400 sample could also contributed to the improvement of the YS. Considering that the precipitates in R400 sample were not obviously

**Table 1**
Mechanical properties and electrical conductivity of BM and FSP samples.

| Sample | Hardness (HV) | YS (MPa) | UTS (MPa) | Total elongation (%) | Electrical conductivity (% IACS) |
|---|---|---|---|---|---|
| BM | 151 ± 4 | 417 ± 1 | 463 ± 2 | 31 ± 1.1 | 80.5 ± 0.3 |
| R600 | 168 ± 4 | 540 ± 3 | 580 ± 4 | 15 ± 0.8 | 70.3 ± 0.8 |
| R400 | 196 ± 6 | 670 ± 3 | 702 ± 5 | 16 ± 0.7 | 74.3 ± 0.9 |

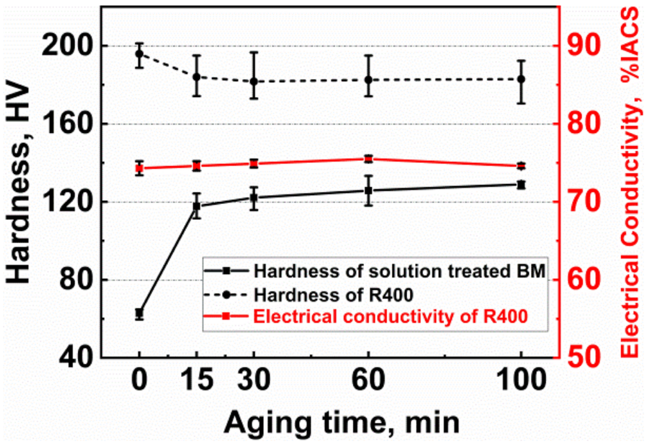


**Fig. 8.** Effect of aging time at 480 °C on hardness of solution treated BM, and hardness and electrical conductivity of R400 sample.

coarsened and some of them maintained the coherent relation with the Cu matrix, it is possible that the precipitation strengthening in R400 sample was not obviously weakened. Therefore, the YS increment of R400 sample was mainly came from the grain-boundary strengthening.

### 3.3. Electrical conductivity

As shown in Table 1, the average conductivity of the BM is 80.5% IACS. The one-step FSP sacrificed the conductivity slightly. The average conductivity changed from 80.5% IACS to 70.3% IACS and 74.3% IACS in the R600 sample and R400 sample, respectively. The aged state Cu-Cr-Zr alloys were subjected to hydrostatic extrusion in Lipińska et al. (2014), the conductivity decreased from 70.2% IACS to 56.6% ICAS. This indicates that the suitable temperature during SPD is necessary to restrain the decrease of conductivity.

According to Matthiessen's rule mentioned in Hou et al. (2017), the resistivity of material can be represented as:

$$\rho = \rho_T + \rho_{solid\ solution} + \rho_{percipitation} + \rho_{defect} \quad (4)$$

where $\rho_T$ is intrinsic lattice resistivity, correlated to temperature; $\rho_{solid\ solution}$ is resistivity from solid solution; $\rho_{percipitation}$ is resistivity due to precipitates and $\rho_{defect}$ is resistivity from GBs, dislocations and vacancies.

Though grain refinement is a factor for electrical conductivity weakening, R400 sample with the finer grains (250 nm) showed a better electrical conductivity than R600 sample. Compared with other kinds of crystal defects, solid solution is the greatest crystal defect to decrease electrical conductivity reported in Li et al. (2007). R600 sample suffered higher thermal cycling during FSP (Fig. 2), which caused more precipitate to dissolve into the Cu matrix, consistent with previous reports. Therefore, the decreased electrical conductivity of R600 sample was dominated by the solid solution. By comparison, only tiny precipitates dissolved into the Cu matrix in R400 sample to damage the electrical conductivity, so the electrical conductivity was higher than that of R600 sample.

To verify if the precipitates re-dissolved into the matrix under the low heat input thermal cycle for R400 sample, post-FSP aging was conducted. Fig. 8 shows the effect of the aging time on the microhardness of the solution treated BM when aging at 480 °C, and the microhardness as well as conductivity of R400 sample. The ever-rising hardness of solution treated BM from 62 HV to 129 HV shows that the selected aging temperature is proper to precipitation strengthening. The hardness of R400 sample before aging was 196 HV and rapid declined in the first 15 min and then remained stable (182 HV). The incipient descent of hardness should be caused by the recovery effect [3]. The conductivity was maintained at ~75% IACS after aging treatment for various time, which proved that Cr and Zr atoms were still in nearly complete precipitation state in R400 sample. Therefore, it is a negligible reduction in strength and conductivity caused by solid solution in R400 sample. In addition, this also indicates that the post-aging treatment was not needed to further improve the mechanical properties.

Tan et al. (2020) reported that product of strength and ductility (PSD) is an important index to exhibit two key roles of strength (UTS) and ductility (total elongation) in structural materials. The comprehensive properties of strength, elongation and electrical conductivity, including the present work and SPD Cu-Cr-Zr alloys reported previously are shown in Table 2. Fig. 9 shows the PSD-electrical conductivity graph that intuitively summarized the date in Table 2. Compared to other SPD Cu-Cr-Zr alloys with preceding solution treatment and subsequent aging treatment, the property matching of R400 sample has reached a higher level.

Based on the above results, it can be concluded that low heat input FSP is an efficient one-step method to optimize the comprehensive properties of the Cu–Cr–Zr alloys. In this method, the hard state Cu-Cr-Zr alloys were deformed via FSP directly, taking the full advantages of the precipitates to refining the grains during plastic deformation process and omitting the preceding solution treatment. On the other hand, the low heat input was benificial to suppress the dissolution of the precipitates, omitting the subsequent aging process. Therefore, the

**Table 2**
Mechanical and electrical properties obtained in the literature and present work.

| Processing route | UTS (MPa) | Total elongation (%) | PSD (GPa %) | Electrical conductivity (% IACS) | Source |
|---|---|---|---|---|---|
| FSP | 702 | 16.0 | 11.23 | 74.3 | Present work |
| | 580 | 15.0 | 8.70 | 70.3 | |
| ST[a] + HPT + AT[b] | 861 | 14.7 | 12.66 | 56.0 | Purcek et al. (2018) |
| | 805 | 13.0 | 10.47 | 61.0 | Purcek et al. (2020) |
| ST + ECAP + AT | 699 | 11.0 | 7.69 | 59.0 | Purcek et al. (2016) |
| | 676 | 11.7 | 7.91 | 73.0 | Liang et al. (2018) |
| | 742 | 9.0 | 6.68 | 70.0 | Purcek et al. (2014) |
| Cold rolling + AT | 648 | 8.2 | 5.31 | 79.8 | Li et al. (2019) |
| | 568 | 9.4 | 5.34 | 75.3 | Meng et al. (2019) |
| | 690 | 1.2 | 0.83 | 67.0 | Zhang et al. (2017) |
| ST + LNT FSP + AT | 840 | 2.5 | 2.10 | 89.0 | Wang et al. (2019) |
| Annealing + LNT DPD[c] | 700 | 4.3 | 3.01 | 78.5 | Sun et al. (2015) |
| Rotary swaging + AT | 612 | 9.4 | 5.75 | 84.7 | Huang et al. (2019) |
| ARB[d] + AT + Cold rolling | 745 | 7.0 | 5.22 | 68.0 | Akita et al. (2010) |

[a] solution treatment,
[b] subsequent aging treatment,
[c] dynamic plastic deformation,
[d] accumulative roll bonding.

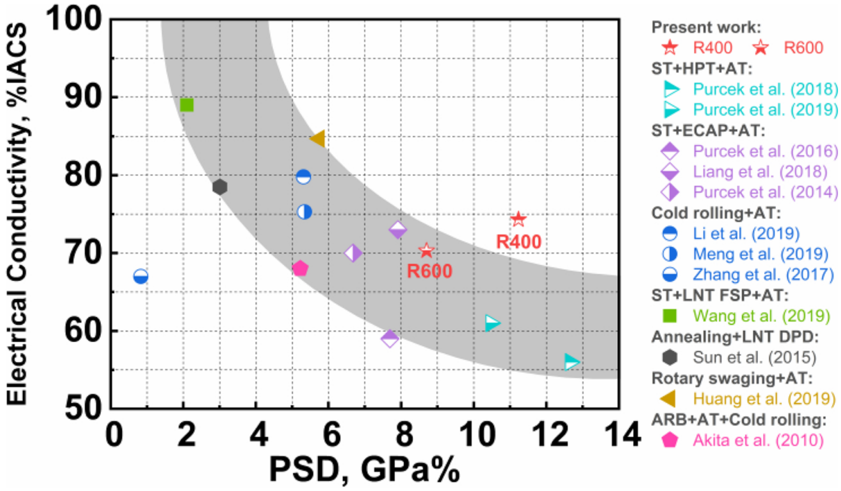


**Fig. 9.** PSD and electrical conductivity comparisons of various Cu-Cr-Zr alloys.

enhanced combination of mechanical properties and electrical conductivity of Cu-Cr-Zr alloys were guaranteed by the UFG structures, nanoscale precipitates, low dislocation density and low-solute-content matrix via one-step FSP.

## 4. Conclusions

In this study, a hard state Cu-Cr-Zr alloy was subjected to FSP at a low heat input with the aim to obtain excellent mechanical properties while maintaining its good electrical conductivity. The microstructures, mechanical and electrical properties of the FSP samples were investigated carefully. The main conclusions and findings can be summarized as follows:

1 During FSP, the peak temperature near the SZ on the AS was 428 °C for R600 sample, and decreased to 240 °C for R400 sample. Under the low heat input condition, UFG microstructure was obtained in a hard state Cu-Cr-Zr alloy, with the grain sizes refined to 360 nm in R600 sample and 250 nm in R400 sample, respectively.
2 Compared to the precipitates in the BM with an average size of 2.8 nm, the precipitates in R600 sample coarsened to an average size of 5.5 nm and part of precipitates dissolved into the matrix. However, the precipitates (average size of 3.1 nm) neither dissolved nor obviously coarsened were obtained in R400 sample, and some of them still maintained the coherent relationship with the Cu matrix.
3 The R400 sample exhibited excellent comprehensive properties of high tensile strength (702 MPa), good ductility (16%) and electrical conductivity (74.3% IACS), and the property matching was higher than that of other SPD Cu-Cr-Zr alloys. The increased comprehensive properties of R400 sample mainly came from the significantly refined grains and the reserved fine precipitates.

## Declaration of Competing Interest

The authors report no declarations of interest.

## Acknowledgement

This work was supported by the National Natural Science Foundation of China under grant No. U1760201, and the Youth Innovation Promotion Association of the Chinese Academy of Sciences (2017236).

## References

Akita, T., Kitagawa, K., Kita, K., Gotoh, M., Hirose, Y., Tsuji, N., 2010. High performance of mechanical and electrical properties of Cu-Cr-Zr alloy sheets produced by ARB process and additional thermo-mechanical treatment. J. Phys: Conf. Ser. 240, 012119.
Chakrabarti, D.J., Laughlin, D.E., 1984. The Cr-Cu (Chromium-Copper) System. Bull. Alloy Phase Diagrams 5, 59–68.
Chbihi, A., Sauvage, X., Blavette, D., 2012. Atomic scale investigation of Cr precipitation in copper. Acta Mater. 60, 4575–4585.
Chembarisova, R.G., Sarkeeva, E.A., Alexandrov, I.V., Wei, W., 2020. Analysis of the effect of equal-channel angular pressing on the strength and electrical conductivity of low-alloyed alloys of the Cu-Cr-Zr system. J. Phys: Conf. Ser. 1431, 012065.
Chen, H.M., Yuan, D.W., Xie, W.B., Zhang, J.B., Wang, H., Yang, B., 2019. A novel route for strengthening copper rods: Non-solution heat treatment combined with pre-aging. J. Mater. Process. Technol. 274, 116290.
Chen, J., Lu, L., Lu, K., 2006. Hardness and strain rate sensitivity of nanocrystalline Cu. Scr. Mater 54, 1913–1918.
Chen, J.S., Yang, B., Wang, J.F., Xiao, X.P., Chen, H.M., Wang, H., 2018a. Effect of different Zr contents on properties and microstructure of Cu-Cr-Zr alloys. Materials Research Express 5, 026515.
Chen, X.B., Jiang, F., Jiang, J.Y., Xu, P., MengTong, M., Tang, Z.Q., 2018b. Precipitation, Recrystallization, and Evolution of Annealing Twins in a Cu-Cr-Zr Alloy. Metals 8, 227.
Hou, J.P., Wang, Q., Zhang, Z.J., Tian, Y.Z., Wu, X.M., Yang, H.J., Li, X.W., Zhang, Z.F., 2017. Nano-scale precipitates: The key to high strength and high conductivity in Al alloy wire. Mater. Des. 132, 148–157.
Huang, A.H., Wang, Y.F., Wang, M.S., Song, L.Y., Li, Y.S., Gao, L., Huang, C.X., Zhu, Y.T., 2019. Optimizing the strength, ductility and electrical conductivity of a Cu-Cr-Zr alloy by rotary swaging and aging treatment. Mater. Sci. Eng. A 746, 211–216.
Jha, K., Kumar, S., Nachiket, K., Bhanumurthy, K., Dey, G.K., 2017. Friction Stir Welding (FSW) of Aged CuCrZr Alloy Plates. Metall. Mater. Trans. A 49, 223–234.
Kulczyk, M., Pachla, W., Godek, J., Smalc-Koziorowska, J., Skiba, J., Przybysz, S., Wróblewska, M., Przybysz, M., 2018. Improved compromise between the electrical conductivity and hardness of the thermo-mechanically treated CuCrZr alloy. Mater. Sci. Eng. A 724, 45–52.
Lai, R.L., Li, X.Q., He, D.Q., Lin, J.Y., Li, J., Lei, Q., 2018. Microstructures evolution and localized properties variation of a thick friction stir welded CuCrZr alloy plate. J. Nucl. Mater. 510, 70–79.
León, K.V., Muñoz-Morris, M.A., Morris, D.G., 2012. Optimisation of strength and ductility of Cu–Cr–Zr by combining severe plastic deformation and precipitation. Mater. Sci. Eng. A 536, 181–189.
Li, H.Q., Xie, S.S., Wu, P.Y., Mi, X.J., 2007. Study on improvement of conductivity of Cu-Cr-Zr alloys. Rare Met. 26, 124–130.
Li, R.G., Guo, E.Y., Chen, Z.N., Kang, H.J., Wang, W., Zou, C.L., Li, T.J., Wang, T.M., 2019. Optimization of the balance between high strength and high electrical conductivity in CuCrZr alloys through two-step cryorolling and aging. J. Alloys Compd. 771, 1044–1051.
Liang, N.N., Liu, J.Z., Lin, S.C., Wang, Y., Wang, J.T., Zhao, Y.H., Zhu, Y.T., 2018. A multiscale architectured CuCrZr alloy with high strength, electrical conductivity and thermal stability. J. Alloys Compd. 735, 1389–1394.
Lipińska, M., Bazarnik, P., Lewandowska, M., 2014. The electrical conductivity of CuCrZr alloy after SPD processing. IOP Conf. Series: Materials Science and Engineering 63, 012119.
Liu, Q., Zhang, X., Ge, Y., Wang, J., Cui, J.Z., 2006. Effect of processing and heat treatment on behavior of Cu-Cr-Zr alloys to railway contact wire. Metall. Mater. Trans. A 37A, 3233–3238.
Lu, L., Shen, Y.F., Chen, X.H., Qian, L.H., Lu, K., 2004. Ultrahigh strength and high electrical conductivity in copper. Science 304, 422–426.

Meng, A., Nie, J.F., Wei, K., Kang, H.J., Liu, Z.J., Zhao, Y.H., 2019. Optimization of strength, ductility and electrical conductivity of a Cu–Cr–Zr alloy by cold rolling and aging treatment. Vacuum 167, 329–335.

Mishnev, R., Shakhova, I., Belyakov, A., Kaibyshev, R., 2015. Deformation microstructures, strengthening mechanisms, and electrical conductivity in a Cu–Cr–Zr alloy. Mater. Sci. Eng. A 629, 29–40.

Mishra, R.S., Ma, Z.Y., 2005. Friction stir welding and processing. Mater. Sci. Eng. R 50, 1–78.

Peng, L.J., Xie, H.F., Huang, G.J., Xu, G.L., Yin, X.Q., Feng, X., Mi, X.J., Yang, Z., 2017. The phase transformation and strengthening of a Cu-0.71 wt% Cr alloy. J. Alloys Compd. 708, 1096–1102.

Pippan, R., Wetscher, F., Hafok, M., Vorhauer, A., Sabirov, I., 2006. The Limits of Refinement by Severe Plastic Deformation. Adv. Eng. Mater 8, 1046–1056.

Purcek, G., Yanar, H., Demirtas, M., Alemdag, Y., Shangina, D.V., Dobatkin, S.V., 2016. Optimization of strength, ductility and electrical conductivity of Cu–Cr–Zr alloy by combining multi-route ECAP and aging. Mater. Sci. Eng. A 649, 114–122.

Purcek, G., Yanar, H., Demirtas, M., Shangina, D.V., Bochvar, N.R., Dobatkin, S.V., 2020. Microstructural, mechanical and tribological properties of ultrafine-grained Cu–Cr–Zr alloy processed by high pressure torsion. J. Alloys Compd. 816, 152675.

Purcek, G., Yanar, H., Saray, O., Karaman, I., Maier, H.J., 2014. Effect of precipitation on mechanical and wear properties of ultrafine-grained Cu–Cr–Zr alloy. Wear 311, 149–158.

Purcek, G., Yanar, H., Shangina, D.V., Demirtas, M., Bochvar, N.R., Dobatkin, S.V., 2018. Influence of high pressure torsion-induced grain refinement and subsequent aging on tribological properties of Cu-Cr-Zr alloy. J. Alloys Compd. 742, 325–333.

Shangina, D.V., Bochvar, N.R., Morozova, A.I., Belyakov, A.N., Kaibyshev, R.O., Dobatkin, S.V., 2017. Effect of chromium and zirconium content on structure, strength and electrical conductivity of Cu-Cr-Zr alloys after high pressure torsion. Mater. Lett. 199, 46–49.

Su, J.Q., Nelson, T.W., McNelley, T.R., Mishra, R.S., 2011. Development of nanocrystalline structure in Cu during friction stir processing (FSP). Mater. Sci. Eng. A 528, 5458–5464.

Sun, L.X., Tao, N.R., Lu, K., 2015. A high strength and high electrical conductivity bulk CuCrZr alloy with nanotwins. Scr. Mater. 99, 73–76.

Tan, X.D., He, H.S., Lu, W.J., Yang, L., Tang, B., Yan, J., Xu, Y.B., Wu, D., 2020. Effect of matrix structures on TRIP effect and mechanical properties of low-C low-Si Al-added hot-rolled TRIP steels. Mater. Sci. Eng. A 771, 138629.

Wang, Y.P., Fu, R.D., Li, Y.J., Zhao, L., 2019. A high strength and high electrical conductivity Cu-Cr-Zr alloy fabricated by cryogenic friction stir processing and subsequent annealing treatment. Mater. Sci. Eng. A 755, 166–169.

Wu, L.H., Hu, X.B., Zhang, X.X., Li, Y.Z., Ma, Z.Y., Ma, X.L., Xiao, B.L., 2019. Fabrication of high-quality Ti joint with ultrafine grains using submerged friction stirring technology and its microstructural evolution mechanism. Acta Mater. 166, 371–385.

Xu, N., Song, Q., Bao, Y., 2018. Investigation on microstructure development and mechanical properties of large-load and low-speed friction stir welded Cu-30Zn brass joint. Mater. Sci. Eng. A 726, 169–178.

Xue, P., Wang, B.B., An, X.H., Ni, D.R., Xiao, B.L., Ma, Z.Y., 2019. Improved cyclic softening behavior of ultrafine-grained Cu with high microstructural stability. Scr. Mater. 166, 10–14.

Xue, P., Wang, B.B., Chen, F.F., Wang, W.G., Xiao, B.L., Ma, Z.Y., 2016. Microstructure and mechanical properties of friction stir processed Cu with an ideal ultrafine-grained structure. Mater. Charact. 121, 187–194.

Xue, P., Xiao, B.L., Ma, Z.Y., 2013. Achieving Large-area Bulk Ultrafine Grained Cu via Submerged Multiple-pass Friction Stir Processing. J. Mater. Sci. Technol. 29, 1111–1115.

Yang, C., Zhang, J.F., Ma, G.N., Wu, L.H., Zhang, X.M., He, G.Z., Xue, P., Ni, D.R., Xiao, B.L., Wang, K.S., Ma, Z.Y., 2020. Microstructure and mechanical properties of double-side friction stir welded 6082Al ultra-thick plates. J. Mater. Sci. Technol. 41, 105–116.

Zeng, X.H., Xue, P., Wu, L.H., Ni, D.R., Xiao, B.L., Wang, K.S., Ma, Z.Y., 2019. Microstructural evolution of aluminum alloy during friction stir welding under different tool rotation rates and cooling conditions. J. Mater. Sci. Technol. 35, 972–981.

Zhang, S.J., Li, R.G., Kang, H.J., Chen, Z.N., Wang, W., Zou, C.L., Li, T.J., Wang, T.M., 2017. A high strength and high electrical conductivity Cu-Cr-Zr alloy fabricated by cryorolling and intermediate aging treatment. Mater. Sci. Eng. A 680, 108–114.

Zhao, Y.H., Zhu, Y.T., Lavernia, E.J., 2010. Strategies for Improving Tensile Ductility of Bulk Nanostructured Materials. Adv. Eng. Mater. 12, 769–778.